Journal of Applied Fluid Mechanics, Vol. 17, No. 11, pp. 2481-2498, 2024.
Available online at www.jafmonline.net, ISSN 1735-3572, EISSN 1735-3645.
https://doi.org/10.47176/jafm.17.11.2607

Monitoring the Wake of Low Reynolds Number Airfoils for Their Aerodynamic Loads Assessment

A. Verma† and V. Kulkarni

Department of Mechanical Engineering, Indian Institute of Technology Guwahati, Guwahati, Assam, 781039, India

†*Corresponding Author Email: anand2016@iitg.ac.in*

ABSTRACT

Experimental investigations are carried out to explore the aerodynamic performance and vortex shedding characteristics of S5010 and E214 airfoil-based wings to provide guidance for the design of MAVs and other low-speed vehicles. Force and wake shedding frequency measurements are carried out in a subsonic wind tunnel in the Reynolds number (*Re*) range of 4×10^4 - 1×10^5. The measurements with increasing *Re* show that the slope of the lift curve in the linear region increases by 14% for S5010, while this increment is 11% for E214. The peak lift coefficient of both airfoils reduces with reducing *Re*. For lower pitch angles, the influence of *Re* on drag coefficients is less significant, but at higher angles, the drag increases as the *Re* drops. Unlike pre-stall mountings, the pitch-down propensity of the airfoil enhances in the post-stall region for high *Re* flows. Moreover, the frequency of shed vortices reduces with rising angle of attack at a given *Re*. In contrast, the Strouhal number almost remains constant with varying *Re* at a fixed angle of attack. For S5010 and E214 airfoils, the Strouhal number is noticed to vary between 0.68 - 0.36 and 0.58 - 0.36, respectively, for pitch angle variation of 12°- 28°. The airfoils show a higher Strouhal number than the bluff body wakes, but this difference decreases for high angles of attack mountings. This finding reveals that the wake structure of the airfoil at a high post-stall angle behaves as bluff body wakes.

Article History

Received January 22, 2024
Revised May 6, 2024
Accepted May 12, 2024
Available online September 1, 2024

Keywords:

Wind tunnel measurement
Low Reynolds number
S5010 and E214 airfoils
Aerodynamic characteristics
Vortex shedding frequency
Strouhal number

1. INTRODUCTION

Low Reynolds number (*Re*) aerodynamics plays a very significant role in the evolution of advanced small scale unmanned aircraft. These vehicles include micro unmanned air vehicle (μUAV), micro air vehicle (MAV), nano air vehicle (NAV), etc., which have various applications in both military and civilian sectors. Due to the limitation of wing dimensions, weight, and power input, such vehicles operate in a flow regime of *Re* below 2×10^5, whereas, the large-scale conventional flight vehicles operate at *Re* greater than 1×10^6 (Mueller, 1999). *Re* is defined as the ratio of inertial force to viscous force in fluid flow and is calculated as $Re = U_\infty c/\upsilon$, where U_∞ is freestream velocity, c is chord length, and υ is the kinematic viscosity of air. In the low *Re* fluid flow, viscous effects are dominant as compared to inertial effects. Accordingly, the boundary layer flow characteristics such as laminar-turbulent transitions, separation point, and reattachment zone vary with the *Re*. Therefore, the aerodynamic behavior of low-speed air vehicles is prominently different from that of high-speed flight vehicles. The overview of flow characterization for flow over an airfoil in this *Re* range (1×10^3 - 2×10^5) was presented by Carmichael (1981). In general, for the flow over an airfoil in the *Re* range from 10^3 to 10^4, the boundary layer remains laminar, and transitioning to turbulent flow is very difficult. The housefly and dragonfly are the insects which fly in this flow regime. Further, in the case of hand-launched sailplanes and gliders, which fly in the range between 1×10^4 to 3×10^4, the flow within the boundary layer is completely laminar, and experiences no reattachment after separation. Moreover, the *Re* from 3×10^4 to 7×10^4 is of major relevance to MAV designers and small-scaled aircraft manufacturers. For the flow with higher *Re* ($7 \times 10^4 \leq Re \leq 2 \times 10^5$) as well flow is laminar over an airfoil which improves its performance, but the presence of separation bubble still remains a hurdle for further performance improvement of some airfoils. Beyond this range, for *Re* > 2×10^5, the performance of the airfoil improves considerably as the size of the laminar bubble diminishes. Thus objects flying with velocities corresponding to *Re* below 2×10^5 encounter numerous problems such as formation of laminar separation bubble, bursting of the

NOMENCLATURE

A	wing surface area	f_d	dominant frequency
AoA	angle of attack	fs	vortex shedding frequency
b	wingspan	l	lift force
c	wing chord	m	pitching moment
C_d	drag coefficient	Re	Reynolds number
C_l	lift coefficient	St_s	Strouhal number
C_l / C_d	lift-to-drag ratio	U_∞	freestream velocity
C_{lmax}	maximum lift coefficient	ρ	air density
$C_{m,0.25c}$	pitching moment coefficient about quarter-chord	υ	kinematic viscosity of air
d	drag force		

separation bubble, flow transition, hysteresis in performance parameters, vortex shedding in the wake etc. Further, these features would have large dependence of *Re* in this flow regime. Hence, many researchers have got motivation to work in this flow regime to understand the aerodynamics of flying objects. Prominent findings, in this regard, are compiled herein.

Gerakopulos et al. (2010) investigated separation bubble characteristics for the NACA0018 airfoil for $8 \times 10^4 \leq Re \leq 2 \times 10^5$. According to their investigations, increasing the *AoA* at a given *Re* leads the separation bubble to progress towards the leading edge, and to drop its length. After certain angle, length rapidly increases and makes the bubble longer in size. The transition from short separation bubble to a long one is known as bubble bursting and usually it occurs at the stall angle of attack, resulting in a substantial loss in lift. Similar separation bubble attributes for various angles of attack were observed for DAE51 airfoil in the *Re* range of $3.9 \times 10^4 \leq Re \leq 1.18 \times 10^5$ (Park et al., 2020). Further, the strong effect of *Re* was seen on the boundary layer characteristics of airfoil. The separation bubble length in terms of displacement thickness drops as the *Re* rises, and the bubble persists at a larger pitch angle (O'Meara & Mueller, 1987; Gerakopulos et al., 2010; Park et al., 2020). As a result, the stall angle as well as the maximum lift coefficient rises with the *Re*. Similarly, a reduction in bubble length was observed for the E387 airfoil with increasing *Re* at a constant *AoA* or when the *AoA* is increased at a constant *Re* (McGhee & Walker, 1988).

In earlier studies, a number of researchers had reported the critical *Re* for various airfoils at which their performance varies significantly. In this regard, Schmitz (1967) investigated the aerodynamic behavior of three airfoils or cross sections viz. flat plate (*t*: 2.9%), cambered plate (*t*: 2.9%, 5.8% camber), and N60 (*t*: 12.41%, 4% camber) at $2 \times 10^4 \leq Re \leq 2 \times 10^5$. The results showed that the maximum lift coefficients of N60 airfoil decrease rapidly with decreasing *Re* below 1×10^5, whereas flat and curved plates were less affected by changing *Re*. Hence, thin flat and camber plates showed better aerodynamic performance as compared to N60 airfoil for $Re < 10^5$. Similar observations are seen in the literature that conventional airfoils have better aerodynamic performance in the form of maximum lift coefficient and the sectional lift-to-drag ratio at $Re > 10^6$ (McMasters & Henderson, 1979; Mueller, 1999). However, their performance decreases rapidly with decreasing *Re* below 10^5. Some other studies conducted for the aerodynamic behavior of airfoils designed for $Re > 5 \times 10^5$, showed rapid performance drop with decrease in *Re* below 5×10^5 due to the presence of laminar separation bubbles (Lissaman, 1983; Mueller, 1985a). Therefore, it is essential to note that most of the conventional airfoils perform better for the $Re > 10^5$; but their performance deteriorates sharply with decreasing *Re* below 10^5. Hence, the selection of airfoils becomes very significant for this flow regime because the thick camber or symmetric airfoils are found to have major hysteresis problems during the measurement of lift and drag forces, mainly due to laminar boundary layer separation or bursting of laminar bubbles (Marchman et al., 1985; Mueller, 1985b; Marchman et al., 1987). Aerodynamic hysteresis in an airfoil signifies the alteration of its aerodynamic properties based on the previous variations in the *AoA*, particularly close to the stall angle. This phenomenon results in the lift, drag, and moment coefficients of the airfoil exhibiting multiple values for a given *AoA*. Typically, it is seen at high *AoA*, hence significantly affecting the stall condition of the airfoil. Moreover, Mueller (1985b) found that hysteresis loop size decreases with increasing *Re* for Lissaman 7769 and Miley M06-12-128 airfoils. However, this correlation between *Re* and hysteresis is not the same for all airfoils, since for the airfoils S1210 and FX 63-137, the size of the hysteresis loop grew with *Re* (Selig et al., 1996a).

Further, the enhanced boundary layer thickness and the separated shear layer around the airfoil affect its aerodynamic performance and also create coherent structures in the wake region (Huang & Lin, 1995; Huang & Lee, 2000; Yarusevych et al., 2006). These structures are responsible for undesirable noise and structural vibrations. The characteristics of these structures depend significantly on the boundary layer behaviour, such as separation bubble size, reattachment location, and turbulent transition. Moreover, different types of vortex-shedding structures were observed in the wake region of airfoil, for both pre and post-stall angle of attack. It was reported that the airfoil wake typically behaves like a bluff body wake at higher angles of attack (Huang & Lin, 1995; Huang & Lee, 2000;). However, the pre-stall region's development is significantly different from that of the bluff body wake (Oertel, 1990). Typically, the dimensionless parameter, such as the Strouhal number, is used to analyse the unsteady phenomenon in the wake. Here, the Strouhal number is related to an oscillation in unsteady flow caused by inertial forces relative to the

change in velocity of fluid particles caused by the convective acceleration in the flow field (Katopodes, 2019). Huang & Lin (1995) recorded wide range of Strouhal numbers for different modes of vortex shedding in the wake region of NACA0012 airfoil, in *Re* regime of 2.5×10^4 to 1.2×10^5. It was found that separated shear layer instabilities affect the evolution of vortex shedding in the airfoil wake. They detected periodic coherent structures in the wake only in case of laminar and turbulent boundary layer separations, without reattachment to the surface.

However, the coherency of shed vortices diminished as the flow transitioned from laminar to turbulent, and as a result, no frequency peak appeared in the wake domain. In contrast, Yarusevych et al. (2006, 2009), observed organized wake structures, downstream of NACA0025 airfoil, for both types of flows, such as laminar flow separation without reattachment and with existence of separation bubbles. The results revealed that, as the *Re* rises and a separation bubble develops, the coherency of the wake pattern and the length scale of these vortices diminish. Similarly, *Re* and separation bubble dynamics were also studied for the wake structures of NACA0018 airfoil (Yarusevych & Boutilier, 2011). In some investigations, the Strouhal number was found to be almost constant with variation of *Re* for the wake of bluff bodies such as cylinder and plate at a position of 90° (Roshko, 1954b; Lienhard, 1966). However, the Strouhal number deviation with *Re* is more significant for airfoil than bluff bodies. Further, the Strouhal number for the wake of symmetric airfoils was noted to be higher in comparison to flat plate and bluff body wake for the same flow regime (Roshko, 1954b; Yarusevych et al., 2009; Yarusevych & Boutilier, 2011). This signifies that more streamlined bodies encounter larger Strouhal number for a given flow conditions. Further, the influence of turbulence intensity on the wake shedding behaviour was also investigated for NACA0012 airfoil (Huang & Lee, 2000). This study demonstrated that vortex shedding frequency does not get affected by the freestream turbulence particularly at high angles of attack and *Re*.

In view of the available literature, most of the researchers have focused on exploring the coherent structure characteristics for the wake of symmetric airfoils such as NACA 0012 (Huang & Lin, 1995; Huang & Lee, 2000), NACA0015 (Gerontakos & Lee, 2005), NACA0018 (Yarusevych & Boutilier, 2011), NACA0025 (Yarusevych et al., 2006, 2009), experiencing wide range of *Re* flows. As a result, the majority of past studies address vortex shedding in the wake of symmetric airfoils or bluff bodies. Therefore, very little focus is given to vortex shedding characteristics in the wake region of thin-cambered airfoils. Hence, the explorations for vortex shedding characteristics of cambered airfoils are still an open area for researchers. Further, various numerical and experimental investigations have been reported to understand the performance of conventional and flat plate airfoils from low to high *Re* flows (Mueller & Batill, 1982; Wang et al., 2014; Winslow et al., 2018). Those airfoils showed hysteresis in the measurement of lift and drag forces at the low *Re* range. In the presence of hysteresis, the aerodynamic coefficients of airfoils are found to be multiple values at a given *AoA*, making it challenging to accurately determine the stall condition of airfoils.

Furthermore, the aerodynamic performance of such a symmetric airfoil becomes lower than a cambered airfoil for MAVs in the range of $Re \leq 1 \times 10^5$. Such effects on the airfoil performance were studied for the various airfoils (NACA0003, 2403, 4403, 6403) at $Re = 2 \times 10^4$ - 1×10^5, and found that the lift coefficient increases with increase in the camber of the airfoil (Winslow et al., 2018). However, raising the camber increases drag also, but still the cambered airfoils perform better than symmetric ones in terms of lift-to-drag ratio and maximum lift coefficient. Similar increase in the camber effect on the performance of flat plate airfoils was also reported (Okamoto et al., 1996; Winslow et al., 2018). It was observed that the aerodynamic performance of conventional airfoils decline rapidly when the *Re* decreases below 10^5 and improves if $Re > 10^6$ (McMasters & Henderson, 1979; Mueller, 1999). Therefore, low-speed vehicles with conventional airfoil wings require more power input to operate for low *Re* operations due to higher amount of drag and limitations on maximum lift incurred. Apart from this, aerodynamic data of some high-performance airfoils, based on wind tunnel testing, also have been reported in previous literature, but they also have their limitations. This data is useful for understanding the effect of *Re* on the airfoil performance for $Re > 10^5$. However, for $Re < 10^5$, the lift and drag data of such airfoils are available only for particular *Re* below 10^5, which is insufficient to quantify performance in the low *Re* region (Lyon et al., 1997; Selig et al., 1989, 1996b).

In view of the above research gap, the goal of the present study is to explore the aerodynamic behavior of low-speed cambered airfoils for various *Re* below 10^5. This exploration seeks to promote the adoption of such airfoils in wing design, ultimately aiming to enhance the operational efficiency of MAVs within low-speed regimes. In this regard, wind tunnel experiments are carried out for two low-speed airfoils, S5010 and E214, to understand the performance characteristics over the low *Re* range of $10^4 < Re < 10^5$. These studies are also extended to investigate the wake flow analysis for those airfoils at different angles of attack and freestream conditions. The details of the test model, experimental setup, and measurements are discussed in the following sections.

2. Experimental Apparatus and Methods

2.1 Wing Models

In the present study, two airfoils, S5010 and E214, have been chosen for the fabrication of a rectangular wing model. The geometry of these airfoils is shown in Fig. 1. Both the airfoils are thin, cambered, produce high lift at lower pitch angles, and belong to the category of low *Re* airfoil family (Selig et al., 1989, 1996b). The chord length and span of the wings are 0.15 m and 0.6 m, respectively. The maximum thickness and cambered of airfoil S5010 are 0.098*c* at 0.276*c* and 0.018*c* at 0.32*c*, respectively (Selig et al., 1996b). For the wing of E214 profile, maximum thickness and cambered are 0.111*c* at 0.331*c* and 0.037*c* at 0.569*c*, respectively (Selig et al., 1989).

Table 1 Key parameters used for the printing process

Parameters	Description
Nozzle temperature	210-235 °C
Printing bed temperature	60-70 °C
Layer thickness	0.08 to 0.12mm (For better surface finish)
Infill pattern type	Grid (to optimize object weight, strength, and printing time)
Infill density	40 to 50 % (Provides stiffness)
Infill speed	30 to 35 mm/s (Usually low for better surface finish)
No. of shells	3-4 (to improve strength of model)
Extruder temperature	215 °C

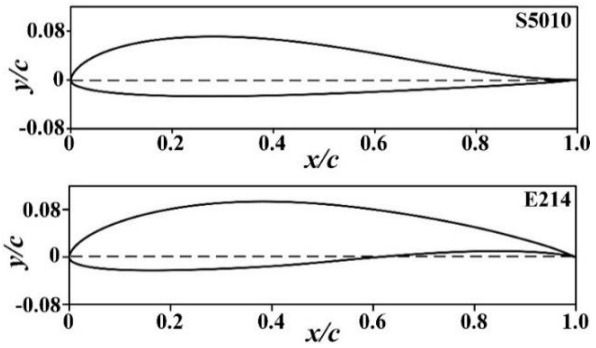

Fig. 1 S5010 and E214 profiles

Thus, the E214 profile is slightly thicker and cambered than the S5010. Since the span of the models covers the entire width of the tunnel test section, there is a minimal to zero gap between the wingtip and tunnel walls. Consequently, the wing tip flow effects are considered negligible in this study and the flow may be characterized as two-dimensional (2D). Similar experimental approach has also been reported in the past where the wing tip flow effects for airfoil are ignored (Selig et al., 1996b; Hu & Yang, 2008; Anderson, 2011).

These models are fabricated from polylactic acid (PLA) material and are printed using a 3D printing machine employing fused deposition modeling (FDM) technology [**Model:** Pro2, **Make:** RAISE3D]. In FDM technology, a thermoplastic filament is heated and extruded layer by layer to create a three-dimensional object. To ensure that the models have a favourable surface finish and better structural stability. A series of assessments has been made on the basis of material layer height, feeding speed, and number of shells. Accordingly, it has been noted that the printing composition of 0.08 - 0.12 mm layer height, 30 - 35 mm/s feed speed, and 3 - 4 nos. of shells produce a good surface finish and structural stability of the model. Some other crucial printing parameters are also detailed in Table 1. The models fabricated under such printing configuration show negligible aerodynamic deviation subjected to low *Re* conditions

2.2 Experimental Setup

Experiments are conducted in an open circuit subsonic wind tunnel at the Department of Mechanical Engineering, Indian Institute of Technology, Guwahati, India. This wind tunnel has square test section of size 600 mm × 600 mm. Schematic of the tunnel is shown in Fig. 2. and its specifications are given in Table 2. Here freestream velocity can be varied from 0.1 m/s to 50 m/s, and it is measured using a pitot static tube connected to an electronic manometer with an uncertainty of ± 0.3%. The pitot-static tube has been placed at about 200 mm from the side wall and about 300 mm from the top and bottom wall of the test section. The resolution of this manometer is 0.01 m/s, and its sampling rate is 100 Hz, which is good enough to define the time average velocity field. For the current studies, this tunnel is calibrated for a wind speed range of 3-15 m/s, where the required velocity is obtained in the test section by changing the tunnel fan rpm. The tunnel calibration curve for the current speed range is given in Fig. 3, where the correlation factor (R^2) = 0.9998. Thus, the linear relationship between tunnel fan rpm (N) and corresponding freestream velocity (U_∞) is evident. For the calibrated wind speed range, the maximum turbulence intensity in the freestream flow is found to be less than 0.35% from the hot wire measurement.

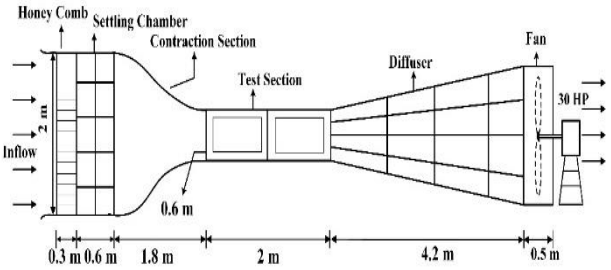

Fig. 2 Schematic of wind tunnel

Table 2 Wind tunnel specifications

Parameters	Details
Tunnel	Open loop suction type
Test section size	2 m × 0.6 m × 0.6 m
Wind speed regime	0.1-50 m/s
Fan rpm range	0-1450
Contraction ratio	9:1
Settling chamber size	1.8 m × 1.8 m
Overall tunnel length	9.4 m
Motor power	30 HP
Turbulent intensity	< 0.35%

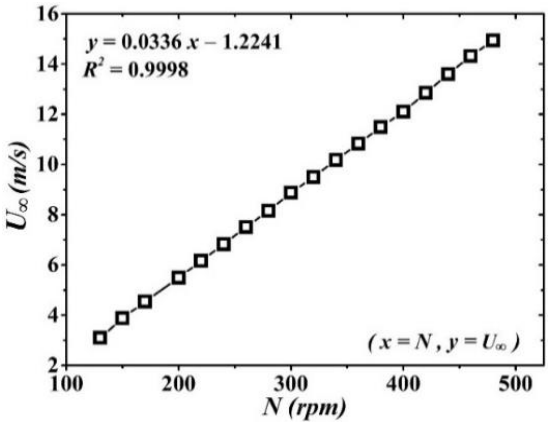

Fig. 3 Wind tunnel calibration curve

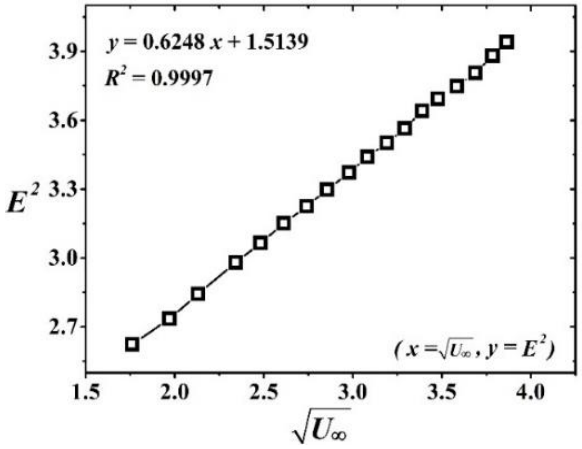

Fig. 4 Hot-wire calibration curve

For the presented investigations, frequencies of wake coherent structure in the airfoil wake are measured using a hot wire anemometer [Model: HWCTA- AMB717, Make: Sunshine Measurements]. It is a constant temperature kind, and the probe wire is made of platinum-coated tungsten with a length of 3 mm and a diameter of 10 μm. The hot-wire probe is typically positioned with its axis perpendicular to the mean flow direction, ensuring uniform heat transfer across its surface. This probe is attached to a holder and mounted on a stepper motor-controlled multi-axis traverse system to perform measurements at a given location. This mechanism allows mobility of the probe in the working section along streamwise (z), vertical (y), and spanwise (x) directions with a resolution of 0.05 mm. The non-dimensional location of the probe in the measurement region is denoted by x/c, y/c, and z/c for the respective directions. The origin of this coordinate system is assumed here to be located at the intersection of the mid-plane of the span and the leading edge of the airfoil at a zero pitch angle. The signals captured by the hot wire are acquired in a data acquisition (DAQ) system [Model: DAQ6363, Make: National Instruments] at a sampling rate of 10 kHz for a sampling time of 10 seconds. This range of sampling frequency not only captures the low and high frequencies of the dissipating vortex but also ensures a negligible aliasing

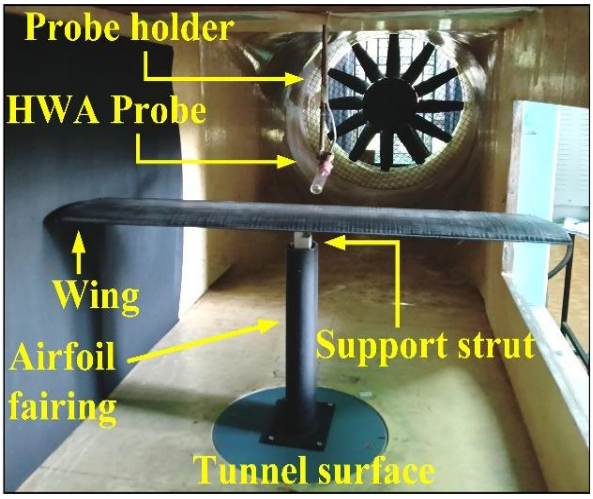

Fig. 5 Model mounted on balance in the test section

effect and maintains the Nyquist-Shannon criteria. Further, the post-processing of the acquired signal is accomplished using the NI-LabVIEW program. The power spectral analysis of the velocity signal is expressed using the mean square amplitude (MSA), and the same is obtained by a fast Fourier transform (FFT) algorithm. For the current study, the anemometer is calibrated for the wind speed of 3-15 m/s by keeping a single probe normal to the flow stream in the test section. The calibration curve is expressed by $E^2 = A + B\sqrt{U_\infty}$ (Bruun, 1995). Figure 4 depicts this calibration curve, where $R^2 = 0.9997$ indicates the linear variation of voltage square (E^2) with the square root of respective velocity ($\sqrt{U_\infty}$).

The aerodynamic forces and moment acting on the wing are measured using a three-component strain gauge balance [Make: WBAL-00103, Model: Sunshine Measurements]. During experiments, the wing models are mounted on a force balance using a support strut structure, which is located at the center of the text section, as shown in Fig. 5. This strut is covered by an airfoil-shaped fairing that is not connected to the balance mechanism. A fairing is a structure that provides streamlined flow due to its airfoil shape and reduces drag. It is fixed to a wooden plate, and it doesn't transmit any force to the balance's measuring mechanism. The strut passes through the fairing without contact and is directly connected to the balance system. Only a small portion of the strut (close to 2.5 cm) is exposed to contact with air. This portion only contributes to drag generation while performing the experiments without mounting the model. The balance essentially measures lift, drag, and pitching moment with maximum capacities of 10 N, 4 N, and 0.5 N-m, respectively. The resolution of the force balance, as specified by the manufacturer, is 0.001 N for lift and drag forces and 0.0001 N-m for a pitching moment. The calibration setup of this force balance is displayed in Fig. 6. The balance is calibrated by placing a known load (W) in the pan, which is connected to the respective strain sensors through a support strut of balance, and the output load is recorded in the microcontroller-based display panel. For lift and pitching moment, the maximum calibration error measured is 3%, and for drag force, it is

Fig. 6 Calibration setup for force balance

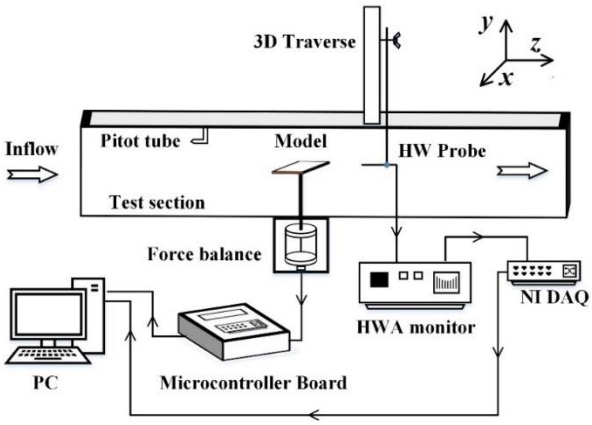

Fig. 7 Experimental setup

found to be 2.0%. In order to obtain the aerodynamic force coefficients, the lift and drag forces are non-dimensionalized using freestream dynamic pressure ($1/2\rho U_\infty^2$) and wing surface area (A). Simultaneously, pitching moment data for each wing model is computed at the quarter chord ($0.25c$) station of the mean chord from the leading edge. It is also non-dimensionalized, employing freestream dynamic pressure, wing area, and mean-chord length.

The complete experimental setup for force measurement and wake study is shown through the schematic in Fig. 7. Here, the balance is attached at the bottom surface of the tunnel, and the wing model is fixed on the top section of balance, using the model support plate. The pitch angle of the mounted model can be varied from –10° to 30° and the same is measured using a digital spirit level with an uncertainty of ± 0.1°. The balancing mechanism is connected to an electronic panel through a wire. This panel is used to convert the instantaneous voltage signal received from strain gauge sensors into respective forces and moments. Further, the output data is stored in a computer that is connected to the balance using an RS232 cable. To study the interference between the support strut and the model, the experiments were also conducted without mounting the wing model on the balance. The lift force generated by the support strut (without the wing model) was found to be close to zero, while the drag force was found to vary from 0.002 to 0.008 N in the tested range of *Re*. However, this magnitude is much lower compared to the drag experienced by the wing model. Therefore, the interference from the support strut is deemed negligible in the force measurements of the model. The lower drag experienced by the strut is mainly due to the use of an airfoil fairing in the balance system, which covers a larger portion of the strut, exposing only a smaller portion to the air.

For obtaining the frequency of shed vortices behind the airfoil, a hot wire probe is placed in the wake region and its movement is controlled by the 3D traverse mechanism, which is mounted at the top of the tunnel. The data acquisition system is used to acquire the output from the hot wire setup. The issue of noise in this study has been properly monitored since the fluctuation in the signal outlines the level of turbulence in the flow. To triangulate and minimize the level of turbulence, the voltage response from the hot-wire unit during the non-flow condition ($U_\infty = 0$) has been captured. The corresponding spectral response of the signal has been processed to outline the level of unwanted frequency response. Thereafter, the corresponding power spectral distribution of the flow signal ($U_\infty \neq 0$) has been mapped and compared with the non-flow signal state. Accordingly, the domain of influence and the unwanted frequency response are removed using the high-pass and band-pass filters. After performing necessary filtering and signal processing, the spectral response of the flow field indicates the presence of a low-frequency vortex (dominant frequency). This low-frequency response is the frequency of the downstream core vortex that occurs during a unit time period and exhibits a peak among all frequencies in the power spectrum. The frequency response of shed vortices is obtained from power spectra of the velocity signal generated by the FFT approach with a maximum deviation of ± 4% for the current flow regimes.

Furthermore, the blockage ratio is an essential parameter in wind tunnel studies, representing the ratio of the wing's frontal area to the cross-sectional area of the tunnel test section. In the present study, the blockage factor varies within the range of 0.87% to 8.55% for *AoA* range of 2° to 20°. As suggested by reported studies (Van Treuren, 2015; Siram et al., 2022), when the blockage factor is below 10%, there is no need for blockage correction in the measurements. In such cases, the interference effects of the model on the airflow are considered to be minimal, and the impact on experimental results is deemed negligible.

To assess the error in measuring aerodynamic coefficients, the standard deviation of the measured samples and subsequent standard error of the mean is estimated (Moffat, 1988). The force balance has a sampling frequency of 100 Hz, and sample acquisition was conducted over a duration of 20 seconds. Measurements are repeated five times at each *AoA*, maintaining consistency across experimental conditions, whether performed on the same day or on different days. The maximum standard errors of the mean are found to be less than ± 3% for lift and moment measurement, while for

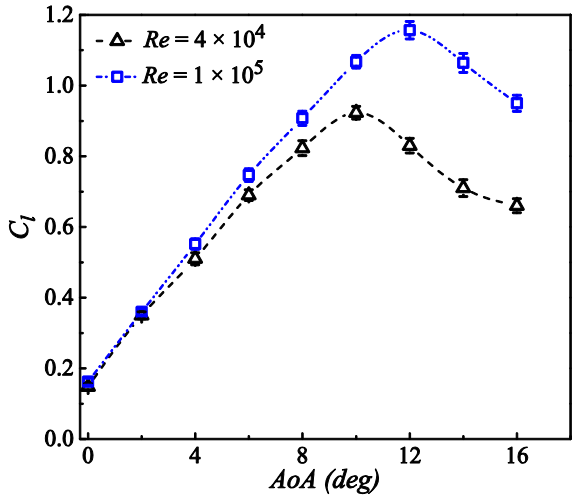

Fig. 8 Error analysis in C_l of S5010 airfoil

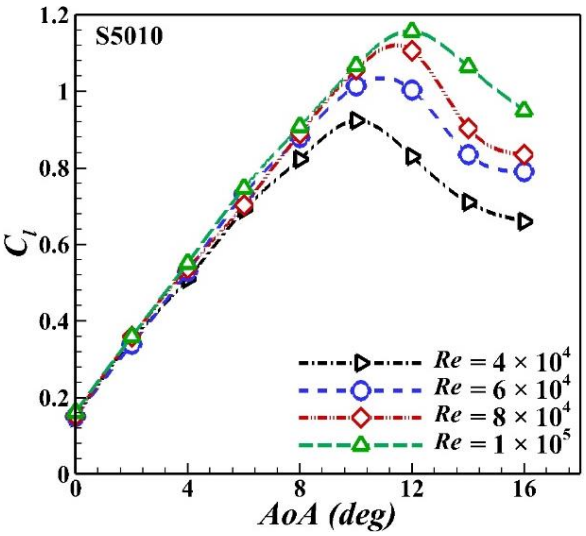

Fig. 10 Lift characteristics at various *Re*

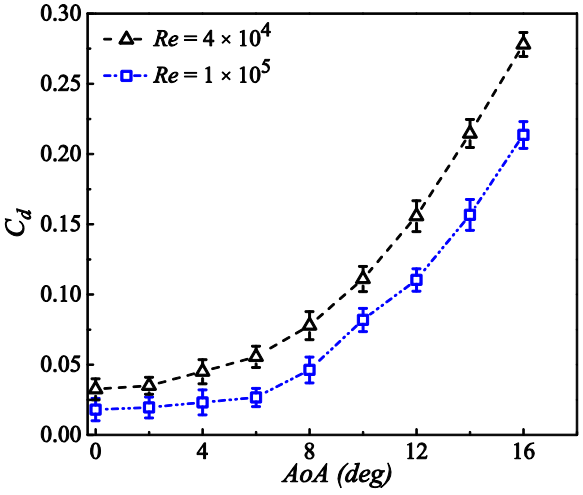

Fig. 9 Error analysis in C_d of S5010 airfoil

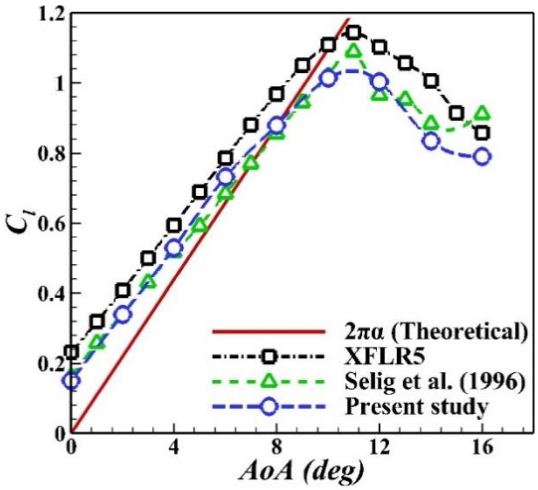

Fig. 11 Validation of present lift coefficient result with the previous investigation at *Re* = 6 × 10^4

drag, it is lesser than ± 1.5%. These estimated errors are represented by the error bars in the lift and drag curve for the two *Re* as 4 × 10^4 and 1 × 10^5, as shown in Figs. 8-9.

3. RESULTS AND DISCUSSION

Experimental studies have been conducted to explore the aerodynamic performance and vortex shedding characteristics of the selected airfoils (S5010, E214) at chord-based Reynolds numbers ranging from 4 × 10^4 to 1 × 10^5. The results are therefore discussed in different sections. The first two sections reveal the analysis of performance (lift, drag, and pitching moment) and frequency of shed vortices in the airfoil wake region for the S5010 profile-based wing model. The next sections discuss aerodynamic behavior and wake region characteristics with respect to the Reynolds number and pitch angle for the E214 wing model. It is known that aerodynamic hysteresis is commonly observed in the force and moment measurements at a high *AoA* for the airfoil. Therefore, experiments are also conducted to study the aerodynamic force and moment data for the existing test models for both rising and falling angles of attack in order to examine the hysteresis, and the same is also addressed separately.

3.1 Performance Analysis of S5010 Airfoil

The experimental results of lift, drag, and moment characteristics as a function of angle of attack (*AoA*) for a wide range of *Re* are shown in Figs. 10-14. Figure 10 reveals the lift coefficient variation with pitch angle from 0° to 16° at *Re* of 4 × 10^4 to 1 × 10^5. The results show that C_L increases with an increased *AoA* up to 10°; after that, it starts to decline rapidly for *Re* = 4 × 10^4. The stall point is detected close to 10°. While, for *Re* = 6 × 10^4, C_L rises up to 11°, after which it starts declining with pitch angle. The current lift coefficient data of *Re* = 6 × 10^4 are compared to Selig's experimental lift results (Selig et al., 1996b) and XFLR5 predictions, as shown in Fig. 11. Here, the solid line represents theoretical lift predictions for an airfoil section wing based on classical thin airfoil theory (Anderson, 2011). Both experimental predictions show slightly higher lift values for the present cambered airfoil as compared to the symmetric airfoil lift values at a low *AoA*. In contrast, the XFLR5 lift predictions show higher

values at each *AoA* from both experimental estimations but still follow a consistent trend of rising and falling of the lift curve with the incidence of stall. Beyond these minor discrepancies, the present lift data shows satisfactory agreement with the reported values.

In the case of $Re = 8 \times 10^4$ - 1×10^5, C_l increases to an angle of 12°, and after that, dropping trends are observed in both cases. So, the stall point is marked as 12°, which is consistent for this *Re* range. Moreover, changing the *Re* has very little effect on the C_l for the pre-stall region but has some effect on the lift value in the post-stall region. At an angle below 8°, the effect of the *Re* is minimal on the lift characteristics. Whereas over 8°, the lift coefficient increases with increasing *Re*. It is found that on reducing the *Re* from 1×10^5 to 4×10^4, the maximum lift coefficient (C_{lmax}) falls by approximately 20%, and the corresponding stall angle decreases from 12° to 10°. However, the variation of C_{lmax} with *Re* for the tested airfoil is low as compared to conventional symmetric airfoil NACA0012 for the same *Re* range. It has been observed that for NACA0012 airfoil, the C_{lmax} decreases approximately up to 23% with a dropping *Re* from 1×10^5 to 4×10^4 (Winslow et al., 2018). Hence, the performance of airfoil S5010 changes less than that of a symmetrical airfoil with a change of *Re* below 10^5. This represents the stability of an airfoil with varying *Re* in this flow regime.

A significant influence of altering *Re* is found on the linear characteristics of the lift curve in the pre-stall region. The performance of the aircraft in terms of control and stability is influenced by the linear or non-linear lift characteristics at small *AoA* in the lift curve (Meng et al., 2018). The present investigations reveal that C_l varies almost linearly with *AoA* up to 8°, after that, non-linear variation is observed for $Re = 4 \times 10^4$. At the same time, this linear region of C_l versus *AoA* is extended to 10° with a larger slope in the case of $Re = 1 \times 10^5$. So, high *Re* shows more linear region in the lift curve for pre-stall angle as compared to low *Re* flows. In the present study, the lift slope values are computed in the linear region of the lift curve using the first derivative of the second-degree polynomial equation with respect to the *AoA*. This polynomial equation is derived from the C_l-curve using the curve fitting procedure. Similar methods were used by Torres and Mueller to calculate the lift coefficient slope for flat plate wings (Torres & Mueller, 2004). According to the conventional thin airfoil theory, the lift coefficient of the airfoil varies linearly with an *AoA*, and the slope of the curve is equal to 2π /rad or 0.11 /*deg*. In the current study, the lift coefficient slope is computed for $0° \leq AoA \leq 6°$ at $Re = 4 \times 10^4$, it is found as 0.085 /*deg*. While for $0° \leq AoA \leq 8°$ and the same *Re*, the lift slope value decreases by 0.08 /*deg*. In the case of $Re = 1 \times 10^5$, the lift slope is noticed as 0.097/*deg* for $0° \leq AoA \leq 6°$ and while it is noted as 0.091 /*deg* for $0° \leq AoA \leq 8°$. Based on the observation, the current lift slope value at $Re = 1 \times 10^5$ is closer to the theoretically predicted slope of 0.011/*deg* than lower *Re* at low *AoA*. Moreover, the lift slope value of the linear region increases by 14% for the change in magnitude of *Re* from 4×10^4 to 1×10^5. Similar behavior of lift slope as a function of *Re* was observed for NACA0012 and cambered plate (5%, camber) at *Re* from 2×10^4 to 7×10^4 (Laitone, 1997).

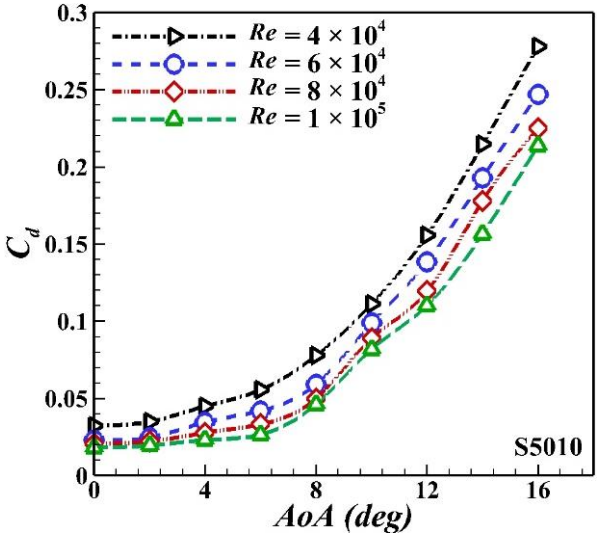

Fig. 12 Drag characteristics at various *Re*

Prior studies have mentioned that the presence of non-linearities in the lift curve is due to the evolution of the laminar separation bubble (LSB) on the suction surface of the airfoil at different *AoA* (Laitone, 1997; Hu & Yang, 2008; Bai et al., 2016). When a separation bubble does not form on the airfoil as usually occurs at small *AoA*, the lift curve remains nearly linear, and the slope of this curve is close to the predicted theoretical slope as 2π. The non-linear effect is found to increase with increasing *AoA*, when a separation bubble is formed on the airfoil. When the *AoA* approaches its critical point, the length of the separation bubble in terms of displacement thickness abruptly increases, which in turn leads to the formation of a larger separation bubble. The transition from a short bubble to a large one is known as bubble bursting, which is directly related to the stall of an airfoil and results in a sudden and significant reduction of peak lift. Moreover, Bai et al. claimed that the abrupt alteration between the long LSB and the trailing edge LSB resulted in a non-linearity in the lift curve of a symmetric airfoil at low *AoA* (Bai et al., 2016). In the current case, the separation bubble is expected to be absent or of small size till the *AoA* of 6° at $Re = 1 \times 10^5$; hence, C_l varies linearly with *AoA*, and the lift slope value is found to be close to the theoretically predicted slope. After the setting of 6°, non-linearity is detected in the C_l-curve and its effect increases continuously with *AoA*, and after the stall point, the lift curve becomes highly non-linear. This signifies the gradual growth of the separation bubble from 6° to 12°, after which the bubble bursts, and consequently, C_l drops dramatically.

Figure 12 shows the drag variation as a function of pitch angle for the *Re* range of 4×10^4 to 1×10^5. The results depict that the drag coefficient increases consistently with *AoA* from 0° to 16°, which is the same for the tested *Re* range. The drag coefficient (C_d) has almost the same value up to the pitch angle of 6°; however, the rate of increase of C_d becomes greater at $AoA \geq 8°$, which is because of higher pressure drag at a high pitch angle. Here, plotted drag data in the C_d - curve is the profile drag of the airfoil, which is the sum of pressure or form

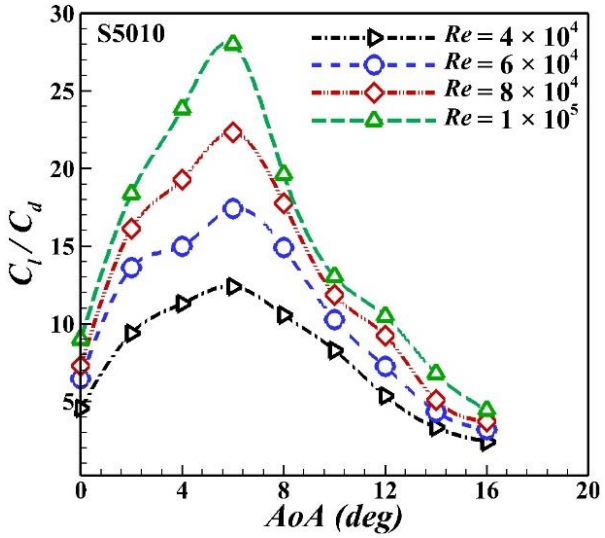

Fig. 13 Lift-to-drag ratio characteristics at various *Re*

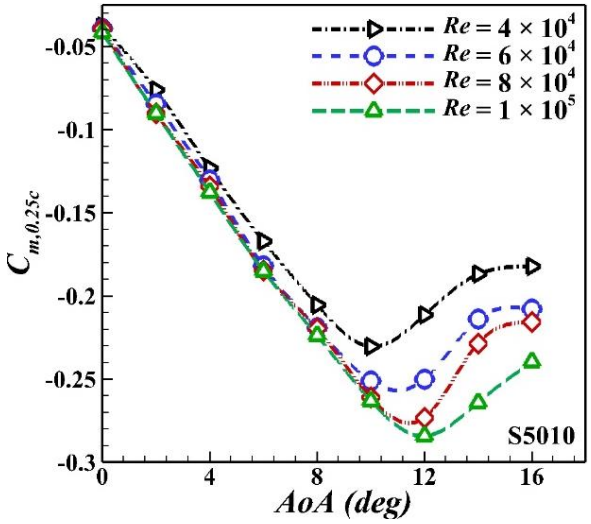

Fig. 14 Pitching moment characteristics at various *Re*

drag (due to flow separation) and skin friction (due to shear stress acting on the airfoil body, depending on the viscosity of fluid and *Re*) (Anderson, 2011). At a low pitch angle, the fluid flow is nearly attached to the airfoil surface, resulting in a low value of form drag. Therefore, the contribution of form drag to the total drag is lesser at low *AoA* than the skin friction drag. Due to this fact, the rate of increase in drag with *AoA* is slower at lower pitch angles. However, as the pitch angle increases, the flow begins to separate from the upper surface, leading to an increase in form drag. As a result, the drag coefficient is observed to increase significantly faster as *AoA* increases. Moreover, Hu and Yang analysed the evolution of separation bubble characteristics and revealed that when the laminar boundary layer was noticed to be strongly attached to the airfoil surface, usually at low *AoA*, then the drag coefficient value appeared to be very small (Hu & Yang, 2008). In contrast, when a laminar separation bubble forms on the airfoil, the drag force increases rapidly with increasing *AoA*. The influence of *Re* on the drag characteristics is observed to be minimal at small *AoA*. However, for $6° \leq AoA \leq 16°$, drag force decreases as *Re* is increased from 4×10^4 to 1×10^5, which indicates the early formation of a separation bubble at low *Re*. Previous studies showed that the laminar separation bubble reduces in length with the increase of *Re*, resulting in a lower value of form drag (O'Meara & Mueller, 1987; Brendel & Mueller, 1988; Gerakopulos et al., 2010). Therefore, the profile drag of the airfoil decreases as *Re* rises at moderate to high *AoA*.

Moreover, lift-to-drag ratio (C_l/C_d) of the S5010 airfoil is estimated for pitch angles from 0° to 16° at a *Re* range of 4×10^4 to 1×10^5, as presented in Fig. 13. An efficient airfoil section provides high lift with minimal generation of drag, so the C_l/C_d measures the aerodynamic efficiency of airfoil. In the present observation, initially, the magnitude of C_l/C_d rises with a rising pitch angle up to a maximum of 6°, after which it continues to decline with angles that are the same for all *Re*. Further, the strong influence of *Re* is noted on the C_l/C_d characteristics of the airfoil. The maximum lift-to-drag ratio $(C_l/C_d)_{max}$ increases from 12 to 28 when *Re* is varied from 4×10^4 to 1×10^5.

The variation of the pitching moment coefficient about a quarter chord ($C_{m,0.25c}$) with a pitch angle in the *Re* range of 4×10^4 to 1×10^5 is illustrated in Fig. 14. The moment coefficient decreases to a negative value with rising angles up to 10°, after this angle, an increasing trend is observed for $Re = 4 \times 10^4$. Similarly, for $Re = 6 \times 10^4$ - 1×10^5, the moment curve reduces up to 12°, then an increasing trend with pitch angle is detected. In this case, the negative pitching moment denotes that when the *AoA* rises, it tends to rotate the wing towards its equilibrium position to counteract the disturbance that arises due to *AoA*. Also, it is mentioned that the slope of the moment curve must be negative for the static longitudinal stability of aircraft (Nelson, 1998).

In the current study, the moment slope is obtained from the linear region of the moment curve and is found in negative values such as –0.0226 /*deg* and – 0.0236 /*deg* at $Re = 4 \times 10^4$ and 1×10^5, respectively. According to Mizoguchi and Itoh, the significance of decreasing pitching moment towards negative values before the stall angle reveals the spreading of the laminar separation bubble over the airfoil surface (Mizoguchi & Itoh, 2013). Here, the pitching moment is caused by normal and axial forces generated by pressure and shear stress distribution over the airfoil surface. An increase in moment value is noted after a particular angle, which is caused by a reduction in lift. Moreover, the influence of the *Re* on the moment characteristics has less significance for the pre-stall region. For the post-stall angle, the magnitude of the pitching moment declines with increasing *Re*; this indicates that the pitch-down tendency of the airfoil becomes higher for high *Re* in the post-stall region.

3.2 Wake Vortex Shedding Analysis of S5010 Airfoil

In the above discussion, it has been observed that the lift characteristics of the S5010 airfoil decline after a pitch angle of 12° for most of the *Re* cases. After *AoA* = 12°, the lift coefficient continues to decrease as the angle

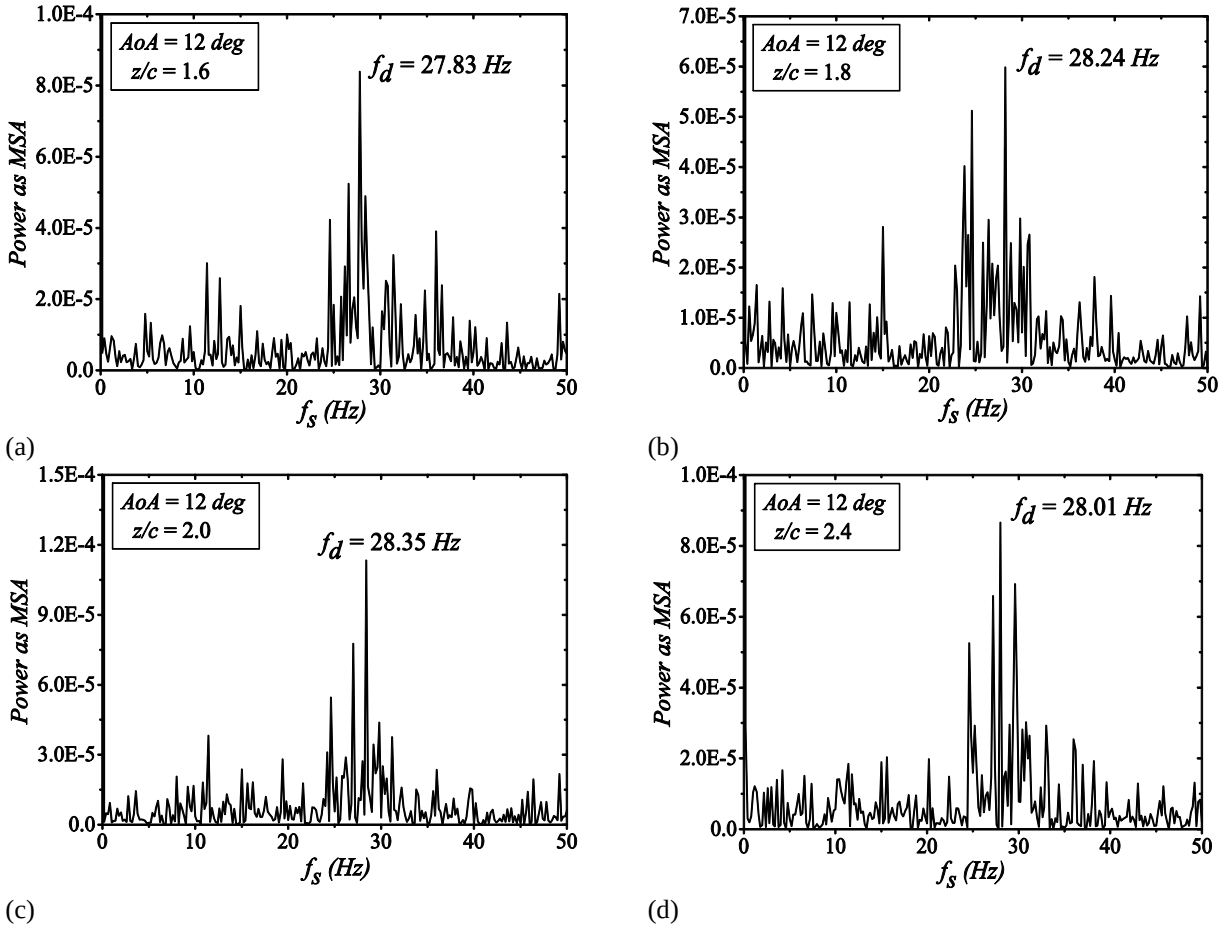

Fig. 15 Frequency response in the wake of S5010 airfoil with the variation of probe locations along streamwise at $Re = 6 \times 10^4$

increases, which signifies that the flow is completely separated from the airfoil surface. These separated shear layers are expected to develop unstable periodic coherent structures in the wake region of an airfoil. Therefore, characterization of the wake is accomplished for vortex shedding frequency and corresponding dimensionless parameter, Strouhal number in the post-stall region ($12° \leq AoA \leq 30°$) and *Re* range of $4 \times 10^4 \leq Re \leq 1 \times 10^5$. In order to measure frequency, the hot wire probe is placed in several positions in the downstream region of the airfoil, including streamwise (*z/c*), across the span (*x/c*), and orthogonal to the stream (*y/c*). The details of the tested wake domain are as follows: $1.5 \leq z/c \leq 2.5$ along the stream direction, while in the vertical direction, it is moved below the leading edge (LE) of airfoil up to $y/c = 0.3$, whereas above LE, it is varied up to $y/c = 0.25$. For the investigation along spanwise, the probe is shifted from quarter to mid-span length ($1.0 \leq x/c \leq 2.0$). The origin of the *x*, *y*, and *z* coordinates system is at the LE of the wing model at zero pitch angle. Initially, to explore the frequency response with the position of the probe in the wake regime, the probe is varied in various locations along the streamwise direction as $z/c = 1.6, 1.8, 2.0, 2.4$ at given $y/c = 0.15$ (above LE), $x/c = 1.2$ (along span). The shedding frequency (f_s) is obtained from the output signal of hot wire through FFT spectral analysis for various streamwise locations corresponding to $AoA = 12°$ and $Re = 6 \times 10^4$, as demonstrated in Fig. 15. The peak of power spectrum represents the dominant frequency (f_d) of shed vortices. Results reveal that no significant variation is observed in dominant frequency with varying probe locations along stream direction from $z/c = 1.6$ to 2.4. However, the amplitude of each spectrum varies with different probe positions. After $z/c = 3.0$ or before $z/c = 1.5$, the hot wire signal becomes irregular, resulting in no dominant frequency peak detected in the power spectrum signal for the S5010 airfoil in the currently tested *Re* and *AoA* ranges. Also, similar tests are carried out for different probe positions normal to the freestream ($-0.3 \leq y/c \leq 0.25$) and for the same pitch angle. No significant variation is found in the vortex shedding frequency for these conditions and set measurement coordinates.

Such experiments are performed for several pitch angles ($12° \leq AoA \leq 30°$) at defined probe location of $z/c = 1.8$, $y/c = 0.15$, $x/c = 1.2$ in the wake at $Re = 6 \times 10^4$ to investigate the influence of pitch angle on the wake field. When the pitch angle is raised from 12° to 28°, the dominant frequency is seen to decline from 28.24 Hz to 14.62 Hz, as depicted in Fig.16. After the pitch angle of 28°, the peak of f_d is found to be constant with angles.

Further, a strong influence of *Re* has been observed on the shedding formation. Figure 17 shows that when the *Re* increases from 4×10^4 to 1×10^5 at given $AoA = 12°$, the frequency peaks in the spectrum shift towards the right from 18.55 *Hz* to 43.58 *Hz*.

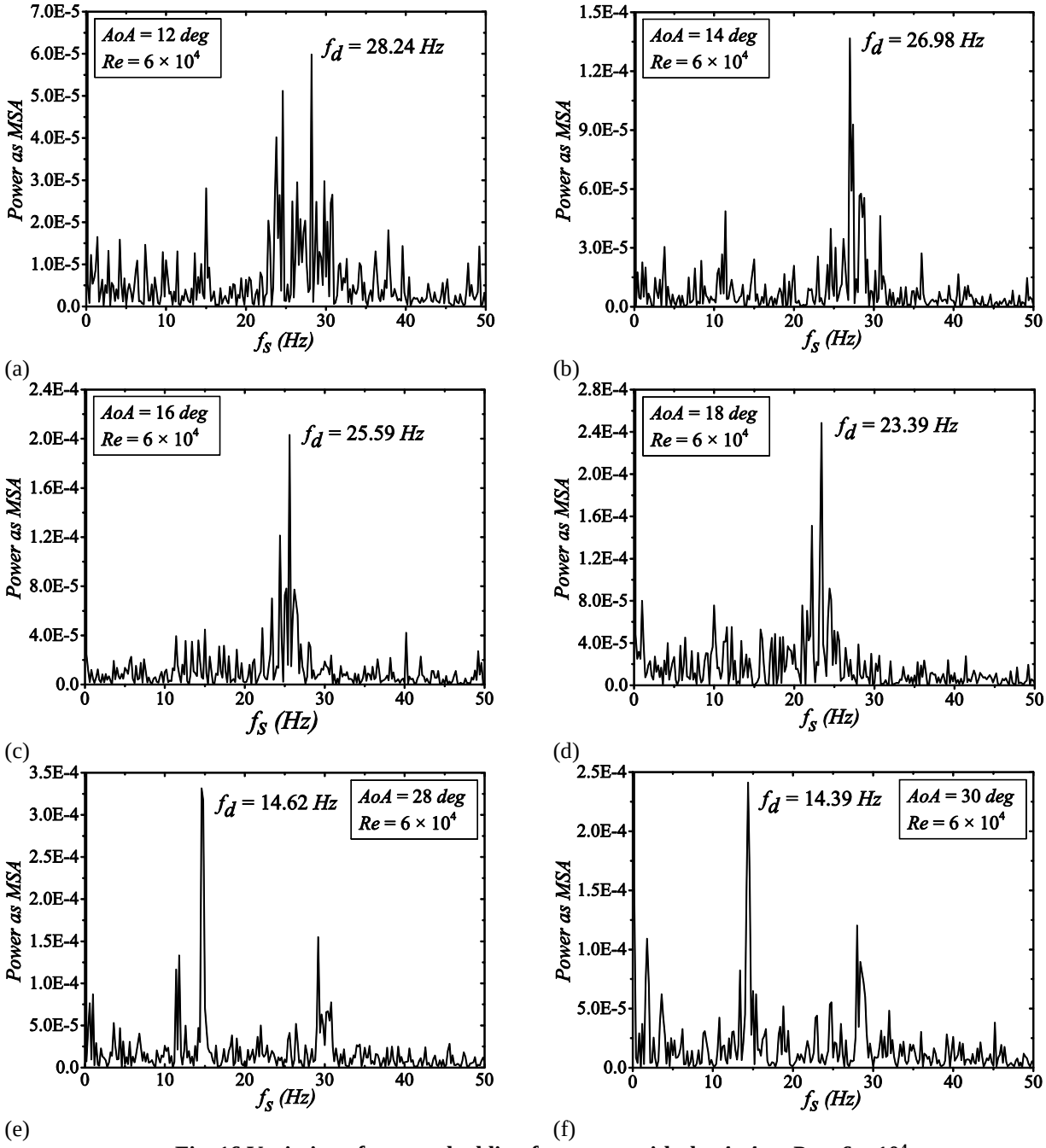

Fig. 16 Variation of vortex shedding frequency with the *AoA* at *Re* = 6 × 10^4

These investigations are also extended to obtain the correlation between shedding frequency, pitch angle, and *Re* for other pitch angles (*AoA* = 16°, 20°, 24°, 28°) and different *Re* ($4 \times 10^4 \leq Re \leq 1 \times 10^5$), as presented in Fig. 18. The analysis of the results shows that the magnitude of the spectral frequency increases linearly with *Re* at a given *AoA*, which is the same for all investigated *AoA* ranges. Despite different flow conditions and experimental parameters, similar linear dependency in the form of $f_s \sim Re$ is observed in the case of symmetric airfoils (NACA0012, NACA0018) and circular cylinders in low *Re* flow regimes (Roshko, 1954a; Huang & Lin, 1995; Yarusevych & Boutilier, 2011).

Further, the Strouhal number (St_s) corresponding to shedding frequency (f_s) is obtained for various *Re* and pitch angles of S5010 airfoil, as demonstrated in Fig. 19. The results show that for a given *AoA*, as the *Re* increases, the shedding frequency also increases but the value of Strouhal number remains almost constant. This can be understood from the fact that the relative change in St_s with respect to an increase in the freestream velocity remains the same, as per the relation, $St_s = f_s\, c/U$. While for a specific *Re*, the St_s decreases as the pitch angle increases. At *AoA* = 12°, the Strouhal number is found to be 0.68 for the *Re* range from 4×10^4 to 1×10^5. However, as the *AoA* increases to 28°, the magnitude of St_s reduces to 0.36 for the same *Re* range. For a pitch angle greater than 25° (*AoA* > 25°), the variation of the Strouhal number with pitch angle shows an almost constant value of 0.36 for the present free stream conditions. As reported, the shedding frequency in the wake region of a bluff body is closely related to wake width and separation angle (Chen & Fang, 1996). Since at a low pitch angle, the airfoil tends to have less divergent flow, thereby generating a narrower width of wake with a shorter time period. Therefore, the vortex

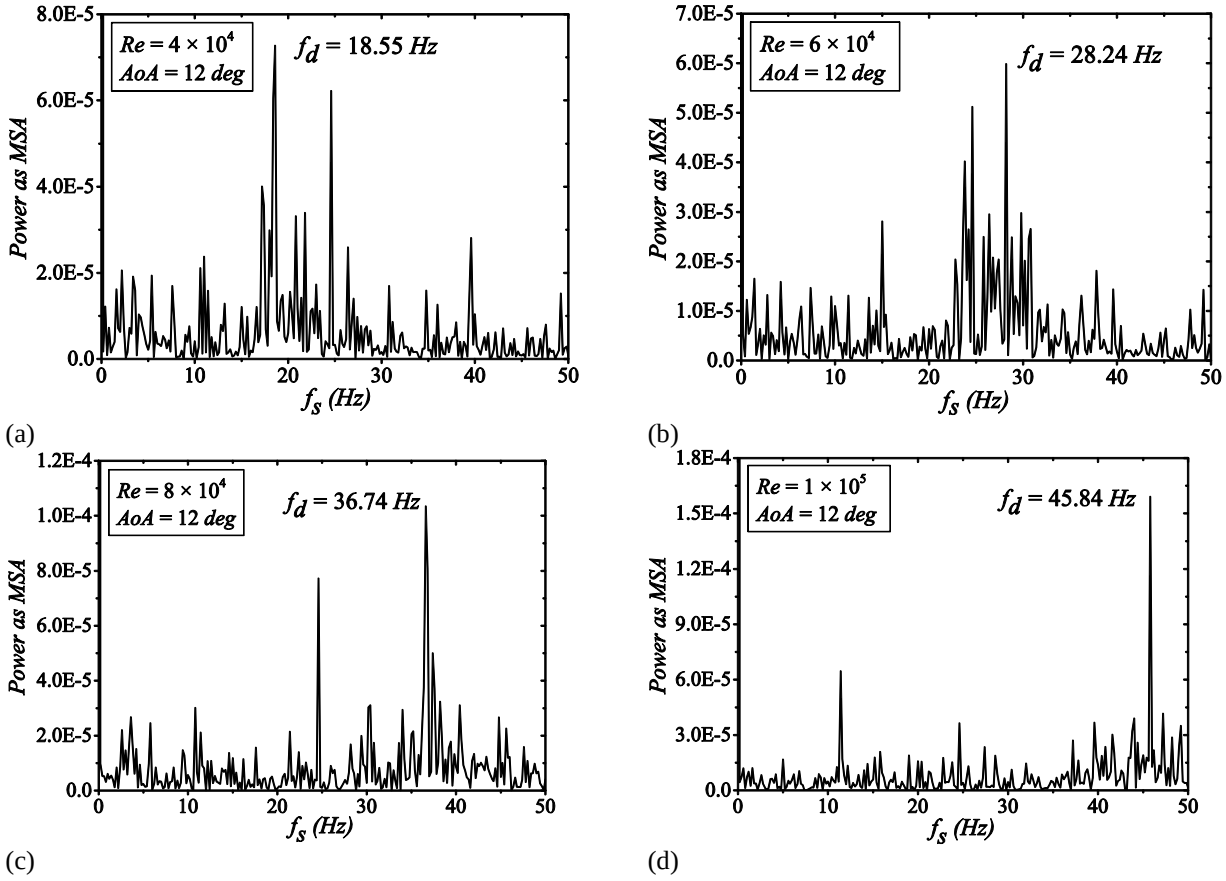

Fig. 17 Vortex shedding frequency response with various *Re* at *AoA* = 12 *deg*

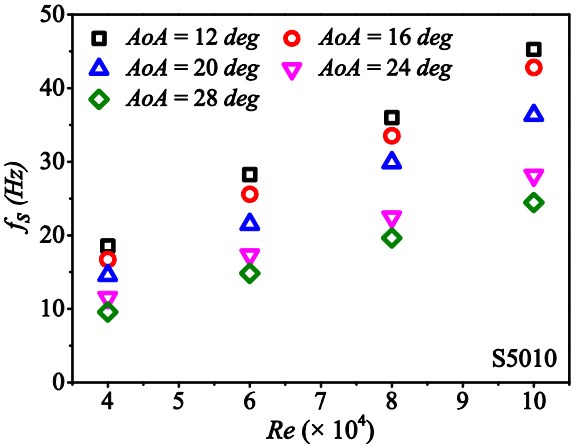

Fig. 18 Variation of vortex shedding frequency with *Re* at various *AoA*

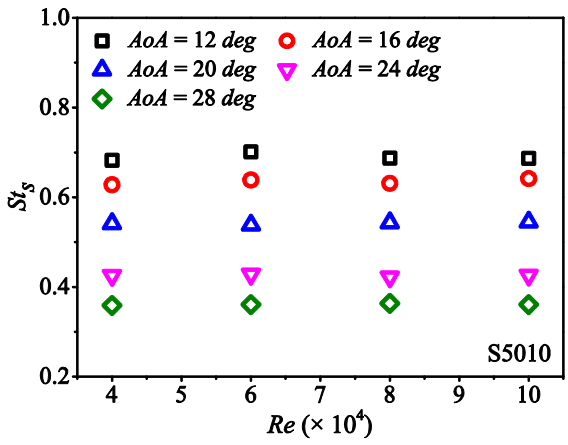

Fig. 19 Variation of Strouhal number based on vortex shedding frequency with *Re* at various *AoA*

frequency and related Strouhal number are higher at a low pitch angle. In contrast, the flow gets more diverged at a high pitch angle, creating wider wake width, thereby obtaining lesser vortex frequency, and this also leads to relatively higher form drag. Thus, it can also be shown that the drag coefficient is directly proportional to wake width and inversely related to the shedding frequency of the airfoil wake. A similar variation of St_s as a function of *Re* and *AoA* was reported for NACA0012 airfoil in the regime of $2 \times 10^4 \leq Re \leq 1 \times 10^5$ at $AoA \geq 15°$ (Huang & Lee, 2000; Huang & Lin, 1995). Similarly, the Strouhal number in the wake of the circular cylinder was also found to be 0.21 for *Re* between 10^4 to 10^5 (Roshko, 1954b; Lienhard, 1966). The St_s for the S5010 airfoil shows a higher magnitude compared to cylinder wake shedding, but as the pitch angle increases, the magnitude difference between them decreases. This result suggested that the wake structure of the airfoil at high-pitch angles behaves as a bluff body wake. As anticipated, the bluff body diverges more flow in the wake as compared to the streamlined body; therefore, the shedding frequency and Strouhal number are higher for an airfoil than a bluff body.

3.3 Performance Analysis of E214 Airfoil

After studying the aerodynamic performance and wake periodicity for the S5010 aerofoil section, similar experiments are performed for the E214 aerofoil. The variation of lift with pitch angles ($0° \leq AoA \leq 16°$) for the

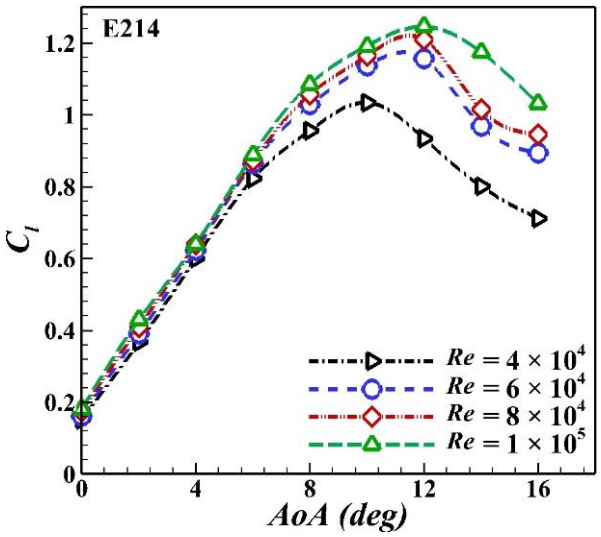

Fig. 20 Lift characteristics at various *Re*

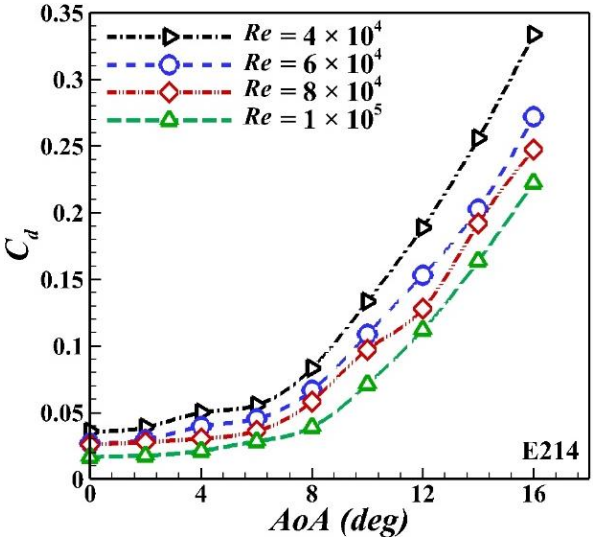

Fig. 21 Drag characteristics at various *Re*

E214 aerofoil section in the *Re* range of 4×10^4 to 1×10^5 is shown in Fig. 20. Figure 20 reveals that lift increases with rising *AoA* till 10°, after which it begins to fall significantly at $Re = 4 \times 10^4$. Whereas in the $Re = 6 \times 10^4$ - 1×10^5, C_l continues to rise with a pitch angle up to 12°; thereafter, a dropping trend is observed for all cases. Thus stall angle of the E214 airfoil is recorded as 10° at $Re = 4 \times 10^4$, while for others *Re*, it is noted as 12°. Further, the influence of *Re* on the C_l is less significant for the pre-stall angle ($AoA < 8°$), but it has a substantial effect at higher pitch angles. For $AoA > 8°$, It is observed that C_l has higher values for higher *Re*. Further, a 17% drop is noted in the C_{lmax} when *Re* is decreased from 1×10^5 to 4×10^4. Winslow et al. found a 23% drop in C_{lmax} for NACA0012 when the *Re* was reduced from 1×10^5 to 4×10^5 (Winslow et al., 2018). In comparison to these conventional airfoils, the peak lift coefficient of the E214 airfoil has a lesser reduction with *Re* below 1×10^5. When compared to the lift data of the S5010 profile, it is found that E214 has a higher value of C_{lmax} at a given *Re*.

Moreover, a substantial effect of *Re* and *AoA* on the linearity of the lift curve is seen at low-pitch angles. The lift curve reveals that C_l varies almost linearly with increasing *AoA* up to 6°, after which non-linear variation occurs for $Re = 4 \times 10^4$. In the case of $Re = 1 \times 10^5$, the linear portion of the lift curve is extended up to *AoA* of 8°. As a result, high *Re* flows exhibit more linear variation of C_l with *AoA* in the lift curve for pre-stall region than low *Re*. Further, the lift curve slope of the linear region ($0° \leq AoA \leq 6°$) is evaluated at $Re = 4 \times 10^4$ and found to be 0.011/*deg*, which is equivalent to the theoretical slope value predicted by thin airfoil theory. For $Re = 1 \times 10^5$, the linear lift slope is estimated as 0.011 / *deg* for the curve portion of $0° \leq AoA \leq 8°$, which is also similar to the theoretical slope of 0.011 /*deg* or 2π /*rad*. As discussed above for S5010, the presence of non-linearity at higher *AoA* in the lift curve is due to the growth of separation bubbles on the upper surface of the airfoil at different *AoA*.

The drag coefficient data as a function of *AoA* ($0° \leq AoA \leq 16°$) for E214 airfoil at *Re* range from 4×10^4 to 1×10^5 is presented in Fig. 21. As per the curve, drag force continues to rise with rising pitch angle, which is consistent for the present *Re* range. However, the magnitude of C_d is almost constant with increasing *AoA* up to 8°, but after this angle, it increases rapidly with *AoA*. This may be due to variation of form drag with different *AoA*. It has also been found that, as the pitch angle exceeds 10°, the form drag increases rapidly. Consequently, the magnitude of C_d rises at a faster rate at high-pitch angles ($AoA \geq 10°$). Furthermore, the effect of *Re* on the drag characteristics is less significant at low pitch angles ($AoA < 8°$) but becomes more effective for $AoA > 8°$. The profile drag of the airfoil decreases with increasing *Re* from 4×10^4 to 1×10^5, which is particularly observed for the *AoA* range from 8° to 16°. The evolution of the laminar separation bubble on the airfoil surface is expected to be early at low *Re* flows, causing higher form drag; therefore, the magnitude of total drag shows higher values at higher *AoA* and lower *Re*. When compared with the drag of the S5010 section, the E214 airfoil exhibits a slightly higher drag value at a high pitch angle for $Re = 4 \times 10^4$, while for $Re = 6 \times 10^4$ - 1×10^5, no significant variation is observed in the drag statistics of these two airfoils even at high *AoA*.

Further, C_l / C_d ratio of the E214 airfoil is evaluated for various pitch angles ($0° \leq AoA \leq 16°$) and *Re* ($4 \times 10^4 \leq Re \leq 1 \times 10^5$) (Fig. 22). The results show that C_l / C_d increases with rising *AoA* up to 6°, then declining trends are observed, that is same for all tested *Re*. The strong effect of *Re* on the lift-to-drag characteristics is observed, an increase of *Re* from 4×10^4 to 1×10^5, the magnitude of $(C_l / C_d)_{max}$ rises approximately from 15 to 31. When compared to the S5010 data, the E214 airfoil has a higher value of $(C_l / C_d)_{max}$ at a given *Re*.

The pitching moment data variation with pitch angles for E214 at different *Re* is demonstrated in Fig. 23. The magnitude of the moment reduces to a negative value with increasing angles up to 10° then it rises rapidly for $Re = 4 \times 10^4$. Similar to this, for $Re = 6 \times 10^4$ - 1×10^5, the moment curve decreases by an angle of 12°, after which an increasing trend is noticed. Rising moment values indicate that the static stability of the airfoil decreases near the stall angle or in the post-stall region. No significant

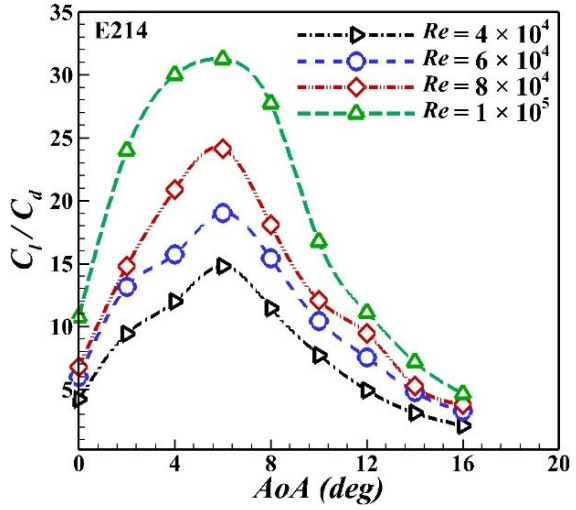

Fig. 22 Lift-to-drag ratio characteristics at various *Re*

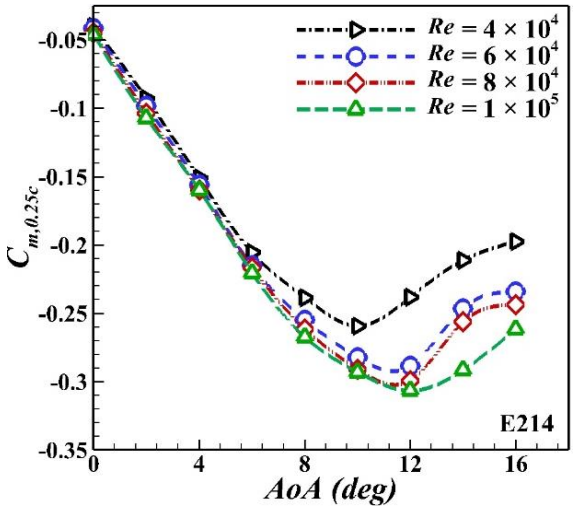

Fig. 23 Pitching moment characteristics at various *Re*

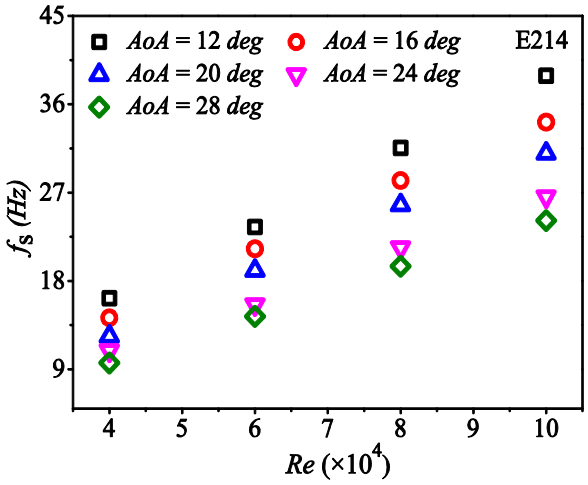

Fig. 24 Variation of shedding frequency with *Re* and *AoA*

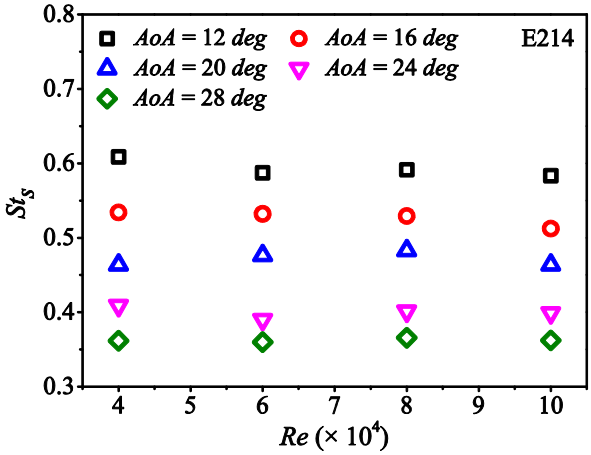

Fig. 25 Variation of Strouhal number with *Re* and *AoA*

effect of *Re* is seen on the moment coefficient for a pre-stall region. However, for the post-stall region, pitching moment data drops with increasing *Re* at a given *AoA*. Comparing two airfoil bodies, the moment characteristics of the E214 profile show slightly higher negative values concerning *AoA* than those of the S5010 airfoil for a given *AoA* and *Re*. This reveals that the pitch-down propensity of E214 is higher than the S5010 section for defined flow conditions.

3.4 Wake Vortex Shedding Analysis of E214 Airfoil

The frequency of shed vortices in the wake region of E214 airfoil for post-stall angle range of $12° \leq AoA \leq 30°$ in a flow regime of $4 \times 10^4 \leq Re \leq 1 \times 10^5$ is measured and presented in Fig. 24. In this analysis, the probe is moved in the wake in all directions, as streamwise ($1.5 \leq z/c \leq 2.5$), orthogonal to stream ($-0.3 \leq y/c \leq 0.2$), and spanwise ($1.0 \leq x/c \leq 2.0$), in order to assess the frequency data. Analysis of the results shows that the shedding frequency remains almost constant with changes in the position of the probe within a marked set of coordinates in the downstream region and for a given *AoA* and *Re*. Further, the variation of sheading frequency with *AoA* and *Re* at a defined probe position of $z/c = 1.8$, $y/c = 1.5$, $x/c = 1.2$ behind the airfoil is shown in Fig. 24. In the case of E214 airfoil, the magnitude of f_s decreases from 23.49 *Hz* to 14.39 *Hz* as *AoA* rises from 12° to 28° at $Re = 6 \times 10^4$. Similar trends ($f_s \sim 1/AoA$) are observed for other *Re*, where the vortex frequency falls as the pitch angle increases, while for $AoA \geq 24°$, this rate of this reduction decreases. In contrast, vortex shedding frequency increases with rising *Re* at a given *AoA*.

The variation of Strouhal number as a function of *AoA* and *Re* in the wake region of the E214 airfoil is shown in Fig. 25. As observed for the S5010 airfoil, the same pattern is noted for E214 airfoil as well where the St_s remains nearly constant with *Re* at a given *AoA* whereas it decreases with *AoA* for specific *Re*.

When comparing the wake periodicities for two airfoils, the St_s for the E214 case reduces from 0.59 to 0.36 with an increase in *AoA* from 12° to 28° at $Re = 6 \times 10^4$, and while in the case of S5010, it decreases from 0.68 to 0.36 for the same flow conditions (Figs. 26-27). The shedding frequency and Strouhal number show a relatively

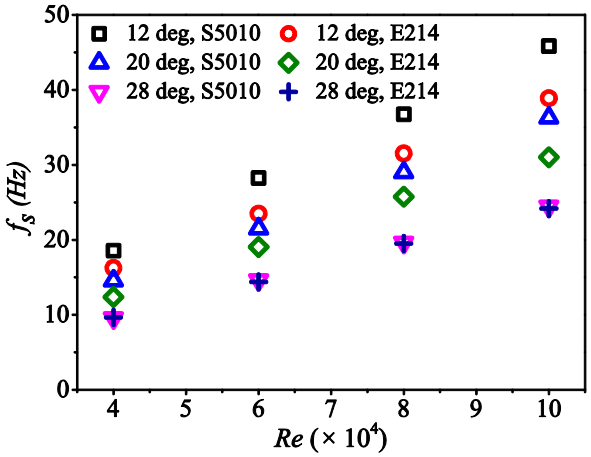

Fig. 26 Comparison of shedding frequencies of S5010 and E214 airfoils

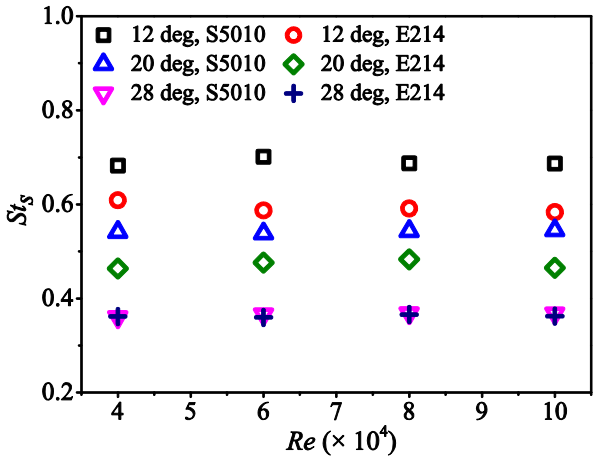

Fig. 27 Comparison of Strouhal numbers of S5010 and E214 airfoils

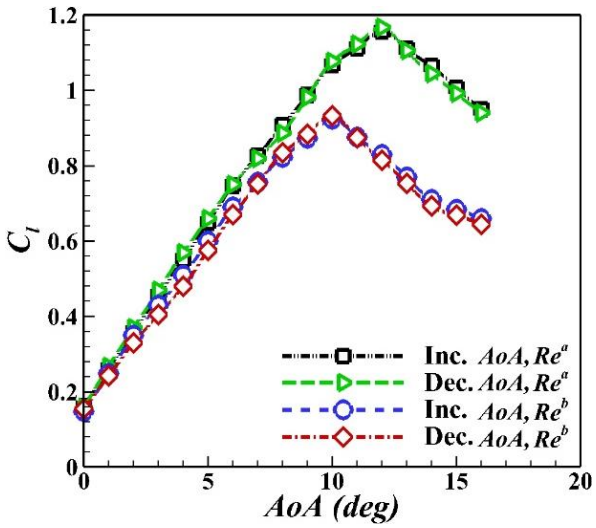

(a) Lift coefficient

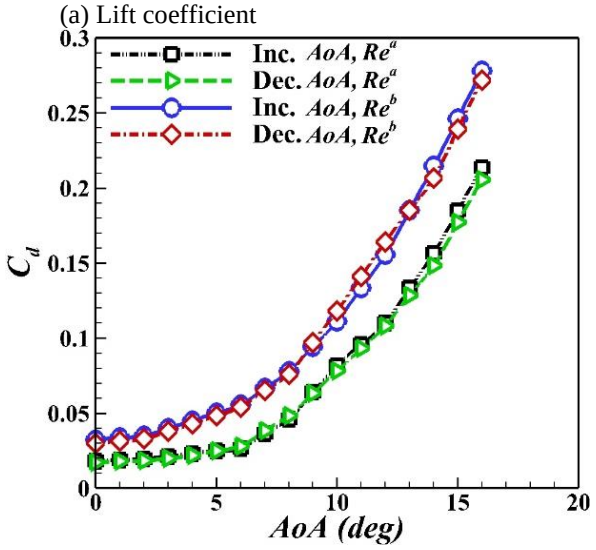

(b) Drag coefficient

Fig. 28 Hysteresis analysis in C_l and C_d for S5010 airfoil

higher magnitude for S5010 than E214 at all $AoA \leq 24°$ in the current freestream range. This is because of the difference in thickness of the airfoils, where S5010 (t/c = 9.8%) is a thinner airfoil than E214 (t/c =11.1%). Thus, the S5010 airfoil diverges the flow less and creates a narrower wake in the downstream region compared to the E214 for *AoA* below 24°, therefore incurring a higher frequency periodic events. But for $AoA > 24°$, both airfoils exhibit almost identical values of frequency and Strouhal number in the measured *Re* range. For $AoA > 24°$, both the airfoil models behave as a bluff body, and the effect of airfoil thickness on the wake structure is diminished. The present finding is consistent with results reported for NACA0018 and NACA0025; thinner airfoils have a higher Strouhal number at a given *Re* and *AoA* (Yarusevych & Boutilier, 2011).

3.5 Results for Aerodynamic Hysteresis Measurement of Airfoils

In order to observe hysteresis in the aerodynamic characteristics of S5010 and E214 airfoils, the wind tunnel investigations are conducted under steady-state or static conditions. For such an experiment, the wing's *AoA* is increased or decreased step by step with a defined interval of angle. In the present study, the *AoA* is set manually using a pitch controller unit (as provided in the balance apparatus) and measured using a digital spirit level. Once the angle was set, readings were recorded for 20 seconds with the model fixed, and then the data were averaged over these readings. After data collection, it is varied to the next *AoA*. The experiments are repeated for a range of *AoA* from 0° to 16° with an interval of 1°. To study the possibility of hysteresis in the data within the tested range of *AoA*, measurements were carried out twice: during the increase of *AoA* (forward sweep) and during the decrease of this angle (reverse sweep). The static approach utilized in this study is a conventional method commonly employed by researchers to analyze hysteresis in aerodynamic studies (Hu et al., 2007; Mizoguchi et al., 2014; Yang et al., 2023).

The lift and drag measurements of the S5010 airfoil with rising and lowering *AoA* in the range of 0° to 16° at two Reynolds numbers, $Re^a = 1 \times 10^5$ and $Re^b = 4 \times 10^4$, are plotted in Fig. 28. The analysis of these figures shows that the magnitude of C_l and C_d with respect to *AoA* is almost similar with increasing *AoA* as that of decreasing angles for the respective *Re*. Moreover, similar

experiments are carried out to examine the hysteresis effect in the force and moment measurement for E214 airfoil at the present *Re* regime. No hysteresis is observed in the aerodynamic data of either airfoil for the current *Re* and *AoA* range. The current finding of the hysteresis effect on the aerodynamic coefficients agrees with the reported observation by Ananda et al. (2012) and Torres and Mueller (2004) for thin profile wings. In their experimental investigations of thin profile wings at low *Re*, they also did not observe any hysteresis in the data and claimed that the small thickness ratio of the wing helps to eliminate the hysteresis.

4. CONCLUSIONS

The present study aims to explore the aerodynamic behavior and wake region characteristics of airfoils for the *Re* range of MAV applications. Regarding this, wind tunnel experiments are successfully carried out on the two rectangular infinite wings of sections S5010 and E214 to obtain the aerodynamic coefficients and wake frequency data in the flow regime of $4 \times 10^4 \leq Re \leq 1 \times 10^5$. In this study, the influence of *Re* and *AoA* on different performance and flow parameters such as linearity of lift curve, lift-to-drag ratio, drag coefficient, pitching coefficient, vortex shedding frequency, and Strouhal number for both airfoils have been discussed. It is noticed that the lift curve depicts more linear variation in the pre-stall region, beyond which, non-linear variation is observed. For S5010, the slope of the lift curve, in the linear region, is found to increase by 14% as *Re* is increased to 1×10^5 for the same *AoA* range. Whereas in the case of E214, this increment is 11%. On reducing *Re* from 1×10^5 to 4×10^4, the peak lift coefficients for S5010 and E214 decrease by 20% and 17%, respectively. These findings demonstrate that the performance of the tested airfoil is less responsive to changes in *Re* below 1×10^5 than a conventional airfoil (Winslow et al., 2018). This reflects the stability of airfoil within a low flow regime with changing *Re*.

The drag magnitude is almost constant at a low pitch angle ($AoA \leq 6°$), after which it increases rapidly, which is expected from the increase in form drag caused by the elongation separation bubble region. Moreover, the *Re* has little effect on the C_d at lower angles ($AoA < 6°$), whereas, for higher angles, the drag increases as the *Re* reduces. The strong influence of *Re* is noticed on the lift-to-drag ratio characteristics of both airfoils; it rises with an improvement of *Re*. For the same *Re*, the magnitude of $(C_l/C_d)_{max}$ is higher for the E214 airfoil compared to the S5010. Here, the pitching moment characteristics are seen to be dependent on the lift values where the magnitude of $C_{m,0.25c}$ decreases towards a negative value (pitch-down) as lift increases with *AoA* up stall point; after that, increasing trends are observed. The effect of *Re* on the $C_{m,0.25c}$ *is* less prominent for the pre-stall region, however, in the post-stall zone, moment data decreases as the *Re* number increases at a given *AoA*. This represents that the nose-down tendency of the wing is higher for high *Re* in the post-stall region. Comparing the moment data of the two airfoils reveals that E214 has a greater negative value than S5010, which indicates that E214 has a higher propensity to pitch down for the same *Re* and *AoA* range.

In order to investigate the behavior of unstable periodic coherent structures in the wake field of airfoils for post-stall angles, the vortex shedding frequency and associated Strouhal number are experimentally estimated for *AoA* range of $12° \leq AoA \leq 30°$ and *Re* of $4 \times 10^4 \leq Re \leq 1 \times 10^5$. The analysis shows that the frequency of shed vortices remains constant with varying probe locations within a defined set of coordinate layouts in the wake domain. This signifies that the wake-shedding structure maintains the same coherency and periodicity within a certain defined region. The magnitude of the shedding frequency and corresponding Strouhal number lower as the *AoA* rises for a given *Re*. The flow gets more diverged at a high *AoA*, creating wider wake width, thereby obtaining lesser vortex frequency, and this also leads to relatively higher form drag. Further, shedding frequency rises linearly with the *Re* in the form of $f_s \sim Re$ at the given *AoA*. At the same time, the Strouhal number remains almost constant with the variation of *Re* for a particular *AoA*. The magnitude of Strouhal number for both the airfoils shows higher values as compared to bluff body wakes, but as the *AoA* increases, the magnitude difference between them decreases. This finding reveals that the wake structure of the airfoil at high *AoA* behaves as bluff body wakes. Comparing the Strouhal numbers of both sections, E214 has a lower magnitude than the S5010 below an *AoA* of 24°. After this angle, both the airfoils show almost identical Strouhal numbers. This is a cause of the thickness of the airfoil; S5010 is thinner than the E214 airfoil. Consequently, the S5010 airfoil diverges the flow less and forms a narrower width of wake in the downstream region than the E214. However, at high angles ($AoA > 24°$), both the airfoil model behaves as a bluff body, and therefore, the effect of airfoil thickness on the wake structure is diminished. Overall, the present investigations not only contribute to the fundamental understanding of low-speed airfoil aerodynamics but also support the integration of such airfoils in MAV wing designs to improve their flying performance in low *Re* regimes.

ACKNOWLEDGEMENTS

The authors are thankful to the funding agency, Aerodynamics Panel of Aeronautics Research and Development Board, India, for funding this project (Project No: 1941).

CONFLICT OF INTEREST

There is no conflict of interest related to the affiliation or involvement of any organization or any entity with a financial or nonfinancial interest in the subject matter or materials discussed in this manuscript.

AUTHORS CONTRIBUTION

Anand Verma: Conceptualization, Experimental Design, Experimentation, Data Collection, Data Analysis, Visualization, Validation, Writing - Original Draft,

Writing - Review & Editing. **Vinayak Kulkarni:** Conceptualization, Supervision, Data Analysis, Validation, Resources, Funding Acquisition, Writing - Review & Editing.

REFERENCES

Ananda, G. K., Sukumar, P. P., & Selig, M. S. (2012). *Low-to-moderate aspect ratio wings tested at low Reynolds numbers*. 30th AIAA Applied Aerodynamics Conference, New Orleans, Louisiana. https://doi.org/10.2514/6.2012-3026

Anderson, J. D. (2011). *Fundamentals of Aerodynamics*. 5th Edition, McGraw–Hill, New York.

Bai, P., Li, F., Liu, Q., & Zhan, H. (2016). *Evolution of the non-linear and unsteady low Reynolds number laminar separation bubble around the airfoil with small angle of attack.* 46th AIAA Fluid Dynamics Conference,Washington, D. C. https://doi.org/10.2514/6.2016-4337

Brendel, M., & Mueller, T. J. (1988). Boundary-layer measurements on an airfoil at low Reynolds numbers. *Journal of Aircraft*, *25*(7), 612–617. https://doi.org/10.2514/3.45631

Bruun, H. H. (1995). *Hot-Wire Anemometry: Principles and Signal Analysis*. Oxford University Press Inc., New York.

Carmichael, B. H. (1981). *Low Reynolds number airfoil survey Vol. 1*. NASA Contractor Report 165803.

Chen, J. M., & Fang, Y. C. (1996). Strouhal numbers of inclined flat plates. *Journal of Wind Engineering and Industrial Aerodynamics*, *61*, 99–112. https://doi.org/10.1016/0167-6105(96)00044-X

Gerakopulos, R., Boutilier, M. S. H., & Yarusevych, S. (2010). *Aerodynamic characterization of a NACA 0018 airfoil at low Reynolds numbers.* 40th AIAA Fluid Dynamics Conference, 1–13. https://doi.org/10.2514/6.2010-4629

Gerontakos, P., & Lee, T. (2005). Near wake behind an airfoil with leading-edge flow control. *Journal of Aircraft*, *42*(2), 561–567. https://doi.org/10.2514/1.9778

Hu, H., & Yang, Z. (2008). An experimental study of the laminar flow separation on a low-Reynolds-number airfoil. *Journal of Fluids Engineering, Transactions of the ASME*, *130*(5), 0511011–05110111. https://doi.org/10.1115/1.2907416

Hu, H., Yang, Z., & Igarashi, H. (2007). Aerodynamic hysteresis of a low-Reynolds-number airfoil. *Journal of Aircraft*, *44*(6), 2083-2086. https://doi.org/10.2514/1.32662

Huang, R. F., & Lee, H. W. (2000). Turbulence effect on frequency characteristics of unsteady motions in wake of wing. *AIAA Journal*, *38*(1), 87–94. https://doi.org/10.2514/3.14382

Huang, R. F., & Lin, C. L. (1995). Vortex shedding and shear-layer instability of wing at low-Reynolds numbers. *AIAA Journal*, *33*(8), 1398–1403. https://doi.org/10.2514/3.12561

Katopodes, N. D. (2019). Viscous Fluid Flow. In K. McCombs, Free-Surface Flow (pp. 324–426). Butterworth-Heinemann. https://doi.org/10.1016/b978-0-12-815489-2.00005-8

Laitone, E. V. (1997). Wind tunnel tests of wings at Reynolds numbers below 70,000. *Experiments in Fluids*, *23*(5), 405–409. https://doi.org/10.1007/s003480050128

Lienhard, J. H. (1966). *Synopsis of lift, drag, and vortex frequency data for rigid circular cylinders.* Bulletin 300. Washington State University, Research Div., Bulletin 300.

Lissaman, P. B. S. (1983). Low-Reynolds-number airfoils. *Annual Review of Fluid Mechanics*, *15*(1), 223–239. https://doi.org/10.1146/annurev.fl.15.010183.001255

Lyon, C. A., Broeren, A. P., Gigu`ere, P., Gopalarathnam, A., & Selig, M. S. (1997). *Summary of Low-speed airfoil data*, Vol 3. SoarTech Publications, Virginia Beach, Virginia.

Marchman, J. F., Abtahi, A. A., Sumantran, V., & Sun, Z. (1985). *Effects of aspect ratio on stall hysteresis for the Wortmann airfoil*. 12th Atmospheric Flight Mechanics Conference, 44–49. https://doi.org/10.2514/6.1985-1770

Marchman, J. F., Sumantran, V., & Schaefer, C. G. (1987). Acoustic and turbulence influences on stall hysteresis. *AIAA Journal*, *25*(1), 50–51. https://doi.org/10.2514/3.9578

McGhee, R. J., & Walker, B. S. (1988). *Experimental results for the eppler 387 airfoil at low reynolds numbers in the langley low- turbulence pressure tunnel*. NASA TM 4062.

McMasters, J. H., & Henderson, M. L. (1979). Low-speed single-element airfoil synthesis. *Technical Soaring*, *6*(2), 1–21.

Meng, X., Hu, H., Yan, X., Liu, F., & Luo, S. (2018). Lift improvements using duty-cycled plasma actuation at low Reynolds numbers. *Aerospace Science and Technology*, *72*, 123–133. https://doi.org/10.1016/j.ast.2017.10.038

Mizoguchi, M., & Itoh, H. (2013). Effect of aspect ratio on aerodynamic characteristics at low Reynolds numbers. *AIAA Journal*, *51*(7), 1631–1639. https://doi.org/10.2514/1.J051915

Mizoguchi, M., Kajikawa, Y., & Itoh, H. (2014). *Static stall hysteresis of low-aspect-ratio wings.* 32nd AIAA Applied Aerodynamics Conference. https://doi.org/10.2514/6.2014-2014

Moffat, R. J. (1988). Describing the uncertainties in experimental results. *Experimental Thermal and Fluid Science*, *1*, 3–17. https://doi.org/10.1016/0894-1777(88)90043-X

Mueller, T. J. (1985a). *Low Reynolds Number Vehicles*. Advisory Group for Aerospace Research and Development, AG-288.

Mueller, T. J. (1985b). The influence of laminar separation and transition on low Reynolds number airfoil hysteresis. *Journal of Aircraft*, *22*(9), 763–770. https://doi.org/10.2514/3.45199

Mueller, T. J. (1999). *Aerodynamic measurements at low Reynolds numbers for fixed wing micro-air vehicles.* RTO AVT/VKI Special Course on Development and Operation of UAVs for Military and Civil Applications, University of Notre Dame.

Mueller, T. J., & Batill, S. M. (1982). Experimental studies of the laminar separation bubble on a two-dimensional airfoil at low Reynolds numbers. *AIAA Journal*, *20*(4), 457–463. https://doi.org/10.2514/6.1980-1440

Nelson, R. C. (1998). *Flight stability and automatic control*. 2nd Edition, McGraw Hill, New York.

O'Meara, M. M., & Mueller, T. J. (1987). Laminar separation bubble characteristics on an airfoil at low Reynolds number. *AIAA Journal*, *25*(8). https://doi.org/10.2514/6.1986-1065

Oertel, H. (1990). Wakes behind blunt bodies. *Annual Review of Fluid Mechanics*, *22*, 539–564. https://doi.org/10.1146/annurev.fluid.22.1.539

Okamoto, M., Yasuda, K., & Azuma, A. (1996). Aerodynamic characteristics of the wings and body of a dragonfly. *Journal of Experimental Biology*, *199*(2), 281–294. https://doi.org/10.1242/jeb.199.2.281

Park, D., Shim, H., & Lee, Y. (2020). PIV measurement of separation bubble on an airfoil at low Reynolds numbers. *Journal of Aerospace Engineering*, *33*(1), 04019105:1-17. https://doi.org/10.1061/(asce)as.1943-5525.0001099

Roshko, A. (1954a). *On the development of turbulent wakes from vortex streets*. NACA-TR-1191.

Roshko, A. (1954b). *On the drag and shedding frequency of two-dimensional bluff bodies.* NACA-TN-3169.

Schmitz, F. W. (1967). *Aerodynamics of the model airplane. Part-1. Airfoil Measurements*. RSIC-721-PT-1.

Selig, M. S., Donovan, J. F., & Fraser, D. B. (1989). *Airfoils at low speeds*. Soartect 8, SoarTech Publications, 1504 North Horseshoe Circle Virginia Beach, Virginia.

Selig, M. S., Guglielmo, J. J., Broern, A. P., & Giguere, P. (1996a). *Experiments on airfoils at low Reynolds numbers.* 34th Aerospace Sciences Meeting and Exhibit. https://doi.org/10.2514/6.1996-62

Selig, M. S., Lyon, C. A., Giguere, P., Ninham, C. P., & Guglielmo, J. J. (1996b). *Summary of low-speed airfoil data*, Vol 2. SoarTech Publications, Virginia Beach.

Siram, O., Kumar, R., Saha, U. K., & Sahoo, N. (2022). Wind tunnel probe into an array of small-scale horizontal-axis wind turbines operating at low tip speed ratio conditions. *Journal of Energy Resources Technology, Transactions of the ASME*, *144*(9), 1–13. https://doi.org/10.1115/1.4053579

Torres, G. E., & Mueller, T. J. (2004). Low-aspect-ratio wing aerodynamics at low Reynolds numbers. *AIAA Journal*, *42*(5), 865–873. https://doi.org/10.2514/1.439

Van Treuren, K. W. (2015). Small-scale wind turbine testing in wind tunnels under low Reynolds number conditions. *Journal of Energy Resources Technology, Transactions of the ASME*, *137*(5), 1–11. https://doi.org/10.1115/1.4030617

Wang, S., Zhou, Y., Alam, M. M., & Yang, H. (2014). Turbulent intensity and Reynolds number effects on an airfoil at low Reynolds numbers. *Physics of Fluids*, *26*(11). https://doi.org/10.1063/1.4901969

Winslow, J., Otsuka, H., Govindarajan, B., & Chopra, I. (2018). Basic understanding of airfoil characteristics at low Reynolds numbers (10^4–10^5). *Journal of Aircraft*, *55*(3), 1050–1061. https://doi.org/10.2514/1.C034415

Yang, Y., Li, C., Pröbsting, S., Liu, X., Liu, Y., & Arcondoulis, E. J. G. (2023). Hysteresis effect on airfoil stall noise and flow field. *Physics of Fluids*, *35*(9). https://doi.org/10.1063/5.0160288

Yarusevych, S., & Boutilier, M. S. H. (2011). Vortex shedding of an airfoil at low Reynolds numbers. *AIAA Journal*, *49*(10), 2221–2227. https://doi.org/10.2514/1.J051028

Yarusevych, S., Sullivan, P. E., & Kawall, J. G. (2006). Coherent structures in an airfoil boundary layer and wake at low Reynolds numbers. *Physics of Fluids*, *18*(4). https://doi.org/10.1063/1.2187069

Yarusevych, S., Sullivan, P. E., & Kawall, J. G. (2009). On vortex shedding from an airfoil in low-Reynolds-number flows. *Journal of Fluid Mechanics*, *632*, 245–271. https://doi.org/10.1017/S0022112009007058